



# The dynamics of non-premixed flames subjected to a transverse acoustic mode

Davy Brouzet<sup>a,b,\*</sup>, Shanni You<sup>a</sup>, Miguel A. Plascencia<sup>c</sup>, Mario Roa<sup>d</sup>, Matthias Ihme<sup>a</sup>

<sup>a</sup> Department of Mechanical Engineering, Stanford University, Stanford, 94305, CA, USA

<sup>b</sup> Center for Turbulence Research, Stanford University, Stanford, 94305, CA, USA

<sup>c</sup> Department of Mechanical and Aerospace Engineering, University of California Los Angeles, Los Angeles, 90095, CA, USA

<sup>d</sup> Sierra Lobo Inc., Air Force Research Laboratory, Edwards AFB, 93524, CA, USA



## ARTICLE INFO

### Article history:

Received 29 March 2022

Revised 8 August 2022

Accepted 10 August 2022

### Keywords:

Non-premixed combustion

Acoustic excitation

Lifted flames

Large eddy simulation

## ABSTRACT

A non-premixed methane/air flame under a transverse acoustic mode is studied by combining theoretical analysis and numerical simulations to understand the acoustic and flow mechanisms affecting the flame response. The experimental configuration under investigation consists of a combustion chamber, a coaxial injector with coflow, and speakers inducing stationary transverse acoustic waves. Numerical simulations reveal a strong response of the flow in the injector to transverse acoustic excitation, resulting in large fluctuations in the mass flow rates of the fuel and oxidizer streams. An analytical model is developed to describe the acoustic response of the flow in the injector to transverse excitation. This model is employed to describe unsteady inflow conditions in large-eddy simulations for different excitation amplitudes. The simulations show that the injector acoustic coupling must be considered to accurately predict the flame lift-off dynamics. Comparisons of numerical results with experimental measurements reveal similar flame structures arising from the longitudinal forcing and good agreement in the lift-off behavior. Further analyses of the flow field, mixing, and flame structure show that the coflow longitudinal forcing induces vortices that corrugate the stoichiometric surface. In addition, the jet forcing enhances the mixing at greater radial locations. The combination of these two mechanisms results in a periodically increased mixing at the stoichiometric surface, leading to significant heat release rate oscillations near the inflow. This work supports the hypothesis that strong acoustic/flame coupling can be present in non-premixed systems when the injectors are longitudinally excited by transverse acoustic waves.

© 2022 The Combustion Institute. Published by Elsevier Inc. All rights reserved.

## 1. Introduction

Combustion instabilities (CIs) are one of the major challenges for the design and operation of gas turbines and rocket engines [1]. These instabilities are characterized by large self-sustaining oscillations in pressure and heat release, arising from the coupling between combustion, acoustics, and unsteady flow field. Recent studies examined CIs in annular combustors to study the nature of transverse modes [2–4] and global flame dynamics [5,6]. More fundamental studies have used acoustic forcing to mimic the acoustic field with either longitudinal [7,8] or transverse [9–11] forcing. Acoustic excitation enables the thorough investigation of the flame and flow behavior and has helped in understanding the physical mechanisms leading to CIs.

When transverse CIs occur, the acoustic field introduces transverse velocity fluctuations inside the combustion chamber and a fluctuating pressure difference between the chamber and the plenum. O'Connor et al. [12] and Urbano and Selle [13] noted that transverse fluctuations do not directly affect the heat release rate in gas turbine and liquid rocket engine configurations. However, pressure fluctuations induce longitudinal waves in burners, nozzles and injectors, which in turn cause heat release fluctuations [14–16]. The acoustic response from different combustor elements are then necessary for the accurate prediction of the injector flow rate and the combustor stability.

Several studies computed the injector or burner velocity fluctuations using linear acoustic models. This enabled the prediction of the combustor stability by describing the flame response with a time-lag model [17,18] or with a numerically-computed and frequency-dependent function [19]. From a configuration point of view, the longitudinal fluctuations inside the injector are drastically affected by the location of the inflow nozzle relative to the acoustic field [20], and by the impedance difference between

\* Corresponding author.

E-mail address: [dbrouzet@stanford.edu](mailto:dbrouzet@stanford.edu) (D. Brouzet).

the plenum and combustion section [19]. Changes in the plenum impedance can significantly affect the combustor stability.

While most studies examined CIs in premixed systems due to their propensity to be more unstable, instabilities have also been observed in partially premixed and non-premixed flames [21–23]. This paper considers two aspects crucial to the understanding of transverse CIs in non-premixed systems: the response of the injector flow to transverse acoustic excitation and the coupling mechanisms occurring in acoustically excited flames.

In a series of experiments [23] and simulations [24] of a Continuously Variable Resonance Combustor (CVRC), it was shown that altering the length of the oxidizer injector in a shear-coaxial combustor affects the combustion stability. From studies on coaxial [25] and swirling [26] non-premixed flames, it was concluded that the greatest inflow perturbations and flame coupling were achieved when resonance occurred in the injector. However, these studies were limited to longitudinal acoustic perturbations. The response of coaxial injectors to transverse acoustic waves and the modification of the resulting flow field have not been examined yet.

Furthermore, most of the literature studied the response of non-premixed flames to longitudinal acoustic forcing. Using an analytical solution to the mixture fraction governing equation, Magina et al. [27,28] showed that longitudinal velocity perturbations lead to vortical disturbances that induce flame wrinkling and local heat release rate fluctuations. The disturbances convect axially at the local flow velocity and decay in amplitude. These studies also noted that heat release rate fluctuations are concentrated near the burner outlet where mixture fraction gradients are highest. These results are supported by experimental findings on laminar flames [8], even though it was noted that natural unstable modes tend to dominate the forced mode, potentially weakening the coupling between heat release and pressure. Forcing these low-frequency buoyancy modes produced large-scale flame structures downstream [29]. Forcing frequencies an order of magnitude larger, which are more likely to be observed in CIs, were found to alter the local mixing and combustion close to the jet exit. Kim et al. [25] examined coaxial, turbulent,  $H_2$ /air flames, showing that large vortical structures in the near field enhanced the mixing.

Increasing inlet flow velocities also induces a flame lifting process. For given coflow conditions, as the fuel mass flow rate is increased, the flame remains attached before it lifts off. If the jet velocity is then decreased, the flame reattaches at a significantly lower amplitude, creating a hysteresis [30,31]. Considering longitudinal acoustic fluctuations of the order of 100 Hz, Baillot and Demare [32] noted that the flame can be lifted when the maximum velocity amplitude is attained and remains lifted during the whole forcing process. Longitudinal forcing can even change the combustion regime depending on the forcing amplitude and frequency [33].

Plascencia et al. [34] are one of the few to have studied non-premixed flames under transverse acoustic modes. This study considered two conditions, in which either the pressure node (PN) or the pressure anti-node (PAN), i.e. the location of the maximum pressure amplitude, aligns with the centerplane of the jet. For PN conditions, they found that the flame becomes more wrinkled but remains anchored even for a large forcing amplitude. In contrast, under a PAN mode, the flame would periodically or completely lift-off and exhibit ‘puff-like’ structures. Detailed numerical studies of acoustically excited turbulent non-premixed flames are lacking in order to explain the flame response mechanisms under longitudinal and transverse excitation.

From the literature, it is clear that transverse acoustic modes can greatly affect the behavior of non-premixed flames. However, longitudinal disturbances resulting from the acoustic response of coaxial injectors are not well documented. The added complexity

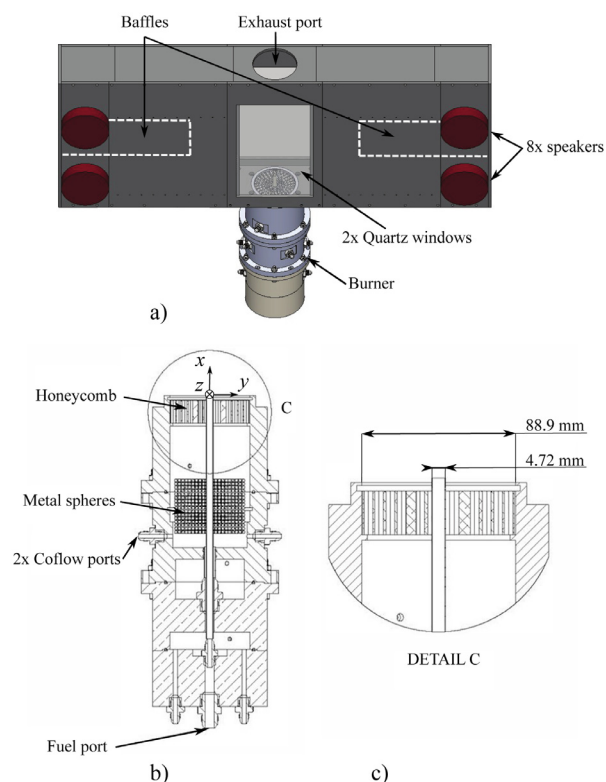


**Fig. 1.** a) Assembly illustrating details of the combustion chamber and injector, b) schematic of the coaxial jet injector with coflow, and c) detailed view of the injector exit.

of this configuration compared to simple injectors requires a thorough analysis and a low order acoustic model is lacking. In addition, our knowledge of how non-premixed flames respond to transverse and longitudinal disturbances is still incomplete. Specifically, the flow, mixing, and combustion processes require further examination to understand their coupling and how they lead to heat release rate fluctuations. This paper addresses these two aspects that are at the core of transverse CIs.

To this end, an acoustic analysis and large-eddy simulations (LES) of the non-premixed burner studied by Plascencia et al. [34] are conducted. The experimental configuration is first presented in Section 2. In Section 3, the numerical methods are discussed. Following this, an analytical model for the acoustic response of the injector is developed, which is subsequently used to prescribe inlet boundary conditions in the LES. Section 4 presents the results, starting by a comparison between the analytical model and simulation results. The LES results of an acoustically forced flame are then compared to available experimental data, particularly focusing on the lifting behavior. Subsequently, the flow, mixing and combustion processes are examined to understand how the non-premixed flame responds to acoustic disturbances. Finally, conclusions are presented in Section 5.

## 2. Experimental configuration

The experiments were conducted at the Air Force Research Laboratory Edwards Air Force Base. Figure 1(a) shows an assembly drawing of the hardware used in this experiment. The injector is located at the bottom of the combustion chamber. The inner dimensions of the aluminum chamber are  $914.4 \times 355.6 \times 108.0$  mm<sup>3</sup>. Two horizontal baffles (dashed white lines) were placed above the chamber floor to suppress vertical acoustic

modes. These baffles are made of aluminum having dimensions of  $254 \times 104.8 \times 3.2 \text{ mm}^3$ .

An exhaust port with a diameter of 88.9 mm is positioned concentrically above the injector. The speakers were threaded directly into the side walls and were attached symmetrically at both ends of the waveguide (4 on each end). One ignition port with diameter of 25.4 mm is located on the back side of the chamber near the bottom wall. Two large rectangular ( $165.1 \times 279.4 \text{ mm}^2$ ) quartz windows provide optical access to the flame and sit flush with the aluminum walls. Nitrogen is purged near the speakers to push the gases inside the chamber towards the exhaust port. This procedure forces the variations in the speed of sound caused by the presence of the flame to remain near the center of the chamber.

Figure 1 (b,c) shows the coaxial jet injector. The injector consists of a center tube (inner diameter  $D_f = 4.0 \text{ mm}$ , length  $L_f = 305 \text{ mm}$ , post thickness  $w_p = 0.36 \text{ mm}$ ) which supplies the fuel (methane). Surrounding the fuel tube is an oxidizer coflow section (outer diameter  $D_c = 88.9 \text{ mm}$ , length  $L_c = 168.4 \text{ mm}$ ) to shield the jet from entrainment and to suppress re-circulation. Quantities associated with the fuel tube and the coflow annulus are denoted by subscripts  $f$  and  $c$ , respectively. The coflow oxidizer was supplied at a velocity of 1 m/s and consists of a mixture of 60% nitrogen and 40% oxygen by mass. Both flows were controlled by choked conditions upstream of the injector using sonic orifices, which provided a constant mass flow rate and well-defined flow and acoustic boundary conditions. The center tube was designed to have a fully developed turbulent flow at the exit.

The Reynolds number in this study ( $Re = 5,300$ ) is evaluated at the fuel injection condition and is based on the tube exit diameter, the bulk velocity ( $U_b = 25 \text{ m/s}$ ), and the fluid properties of methane calculated at atmospheric chamber conditions. To achieve a uniform coflow, the flow was passed through a honeycomb and metal spheres. The honeycomb has a diameter of 88.0 mm and is 25.4 mm thick, with a cell to thickness ratio of 8:1.

### 3. Methodology and mathematical models

In Section 3.1, we first describe the methodologies for the acoustic simulation and LES. To model the unsteady inflow boundary conditions, we then develop an analytical model for the acoustic response of the coaxial injector in Section 3.2. Finally, we present the configurations considered for the acoustic simulation and the LES of the reacting flow in Section 3.3.

#### 3.1. LES equations

To analyze how the acoustic field couples to the flame dynamics, LES are conducted in this work. A fully compressible finite-volume solver [35,36] is used to conduct the simulations. It solves the following Favre-filtered governing equations for conservation of mass, momentum and energy:

$$\partial_t \bar{\rho} + \nabla \cdot (\bar{\rho} \tilde{\mathbf{u}}) = 0 \quad (1)$$

$$\partial_t (\bar{\rho} \tilde{\mathbf{u}}) + \nabla \cdot (\bar{\rho} \tilde{\mathbf{u}} \tilde{\mathbf{u}}) = -\nabla \bar{p} + \nabla \cdot \bar{\boldsymbol{\tau}}_{v+t} \quad (2)$$

$$\partial_t (\bar{\rho} \tilde{e}_{tot}) + \nabla \cdot [\tilde{\mathbf{u}} (\bar{\rho} \tilde{e}_{tot} + \bar{p})] = \nabla \cdot (\bar{\boldsymbol{\tau}}_{v+t} \cdot \tilde{\mathbf{u}}) - \nabla \cdot \bar{\mathbf{q}}_{v+t} \quad (3)$$

with density  $\rho$ , gas velocity vector  $\mathbf{u} = [u, v, w]^T$ , pressure  $p$ , specific total energy  $e_{tot}$ , stress tensor  $\boldsymbol{\tau}$  and heat flux  $\mathbf{q}$ . Overbars and tildes denote Reynolds and Favre filtering, respectively. Subscripts  $v$  and  $t$  denote viscous and turbulent contributions, respectively.

The flamelet/progress-variable (FPV) approach [37,38] is used to model the combustion process in which the thermochemical properties are a function of mixture fraction  $\tilde{Z}$ , progress variable  $\tilde{C}$  and

mixture fraction variance  $\tilde{Z}''^2$ . The solved LES equations for these quantities are as follows:

$$\partial_t (\bar{\rho} \tilde{Z}) + \nabla \cdot (\bar{\rho} \tilde{\mathbf{u}} \tilde{Z}) = -\nabla \cdot \bar{\mathbf{j}}_{Z,v+t} \quad (4)$$

$$\partial_t (\bar{\rho} \tilde{C}) + \nabla \cdot (\bar{\rho} \tilde{\mathbf{u}} \tilde{C}) = -\nabla \cdot \bar{\mathbf{j}}_{C,v+t} + \bar{\omega}_C \quad (5)$$

$$\partial_t (\bar{\rho} \tilde{Z}''^2) + \nabla \cdot (\bar{\rho} \tilde{\mathbf{u}} \tilde{Z}''^2) = -\nabla \cdot \bar{\mathbf{j}}_{Z''^2,v+t} \quad (6)$$

An assumed beta PDF is used to model the subgrid fluctuations in  $\tilde{Z}$  and  $\tilde{C}$  so that the progress variable source term  $\bar{\omega}_C = \bar{\omega}_C(\tilde{Z}, \tilde{C}, \tilde{Z}''^2)$ . The diffusive and turbulent fluxes for the scalar  $\Psi$  are computed as  $\mathbf{j}_{\Psi,v} = -\rho D_\Psi \nabla \Psi$  and  $\mathbf{j}_{\Psi,t} = -\mu_t / Sc_t \nabla \Psi$ , respectively, where  $D_\Psi$  is the diffusion coefficient,  $\mu_t$  is the subgrid scale viscosity and  $Sc_t$  is the turbulent Schmidt number. The system is closed with the ideal gas equation of state.

The equations are discretized using a hybrid scheme that combines a 4th order accurate central spatial scheme with a 2nd order ENO reconstruction scheme in regions of high density gradients [36]. A strong stability preserving 3rd order Runge-Kutta scheme is employed for time-advancement with a maximum CFL number of 1.5.

#### 3.2. Acoustic model for the inlet boundary conditions

In this section, we develop an analytical model to describe the acoustic response of the coaxial injector to transverse acoustic waves in the chamber. The following analysis assumes that the acoustic wavelength,  $\lambda$ , is large compared to the injector diameters, so that only planar waves are present. The most restrictive condition is therefore imposed by the coflow diameter  $D_c/\lambda \leq 0.61$  [39], providing a constraint for the frequency of  $f \leq 0.61c/D_c \simeq 2350 \text{ Hz}$ , with  $c$  being the speed of sound in the injector. The highest frequency considered in this study is equal to 1150 Hz and therefore the longitudinal waves in the injector are assumed to be planar. With this, the pressure and streamwise velocity fluctuations in the injector can be written as a function of the upstream and downstream propagating acoustic wave amplitudes  $A^-$  and  $A^+$ , respectively:

$$p'(x, t) = \Re \{ [A^+ \exp(jkx) + A^- \exp(-jkx)] \exp(-j\omega t) \} \quad (7a)$$

$$u'(x, t) = \frac{1}{\rho c} \Re \{ [A^+ \exp(jkx) - A^- \exp(-jkx)] \exp(-j\omega t) \} \quad (7b)$$

where  $j$  represents the imaginary unit,  $k = 2\pi f/c$  is the wavenumber,  $\omega = 2\pi f$  is the angular frequency and  $\Re\{\cdot\}$  means that only the real part is considered.

We first consider the response of the coflow. The transverse waves generated by the speakers will diffract in the coflow annulus, leading to an upstream propagating wave of amplitude  $A_c^- = \Delta p$ , equal to the combined amplitudes of the two transverse waves in the chamber. As the boundary condition at the bottom of the annulus  $x = -L_c$  is fully reflective, an upstream propagating wave of amplitude  $A_c^+$  will be created. A schematic of the waves is shown in Fig. 2. Solving Eq. (7) by applying the wall boundary condition  $u'_c(-L_c, t) = 0$  leads to the following solution at the coflow exit,

$$p'_c(0, t) = \Delta p \Re \{ [\exp(2jkL_c) + 1] \exp(-j\omega t) \} \quad (8a)$$

$$u'_c(0, t) = \frac{\Delta p}{\rho c} \Re \{ [\exp(2jkL_c) - 1] \exp(-j\omega t) \}. \quad (8b)$$

Equations (8a) and (8b) show that the pressure and velocity at the coflow annulus exit have an amplitude and phase difference

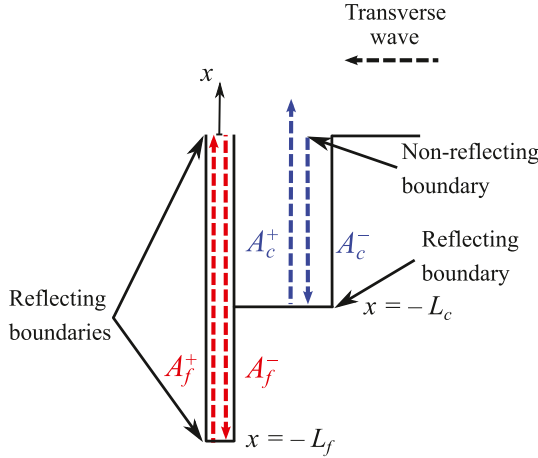


**Fig. 2.** Schematic of the acoustic waves in the coaxial injector. The blue and red dashed arrows represent the waves in the coflow annulus and jet tube, respectively. (For interpretation of the references to colour in this figure legend, the reader is referred to the web version of this article.)

relative to the incoming transverse waves, which is a function of the annulus length  $L_c$ .

As it will be confirmed and discussed in Section 4.1, the downstream propagating wave will then diffract into the combustion chamber, with negligible reflection back into the coflow annulus. Considering our model, this means that the pressure at the fuel nozzle is imposed by Eq. (8a), which can be written as,

$$p_f'(0, t) = \Delta p_f \Re\{\exp(-j\omega t + \phi)\} \quad (9)$$

where  $\Delta p_f = \max[p_c'(0, t)]$  and  $\phi$  are the amplitude and phase of the pressure fluctuations. The condition of zero pressure differential across the nozzle is a well-known result for sharp-edge open pipes with small diameters [40].

We therefore have an acoustic problem in the fuel tube with the two following boundary conditions; the upstream propagating wave with amplitude  $A_f^-$  is reflected at  $x = -L_f$  by the choked flow condition, and the downstream propagating wave with amplitude  $A_f^+$  is reflected by the imposed harmonic pressure condition at the fuel tube outlet (Eq. (9)). To analytically solve this problem of reflected waves both at the bottom and at the top of the fuel tube, the method of characteristics is used [41]. This method leads to the following solution for the downstream and upstream propagating waves,

$$A_f^- = \Delta p_f \Re\left\{\sum_{n=0}^{N_1} (-1)^n \exp(2jknL_f)\right\} \quad (10a)$$

$$A_f^+ = -\Delta p_f \Re\left\{\sum_{n=1}^{N_2} (-1)^n \exp(2jknL_f)\right\} \quad (10b)$$

where the integers  $N_1 = \lfloor (ct + x)/2L_f \rfloor$  and  $N_2 = \lfloor (ct - x)/2L_f \rfloor$  act as counters for the reflected waves. Knowing the analytical form of the geometric series, one can combine Eqs. (7b) and (10) to express the velocity fluctuations at the fuel tube outlet,

$$u_f'(0, t) = -\frac{\Delta p_f}{\rho c} \Re\left\{\left[\frac{1 + (-1)^{N_1} \exp[2jk(N_1 + 1)L_f]}{1 + \exp(2jkL_f)} + \exp(2jkL_f) \frac{-1 + (-1)^{N_2} \exp(2jkN_2L_f)}{1 + \exp(2jkL_f)}\right] \exp(-j\omega t + \phi)\right\} \quad (11a)$$

where  $N = N_1 = N_2$  and the pressure fluctuations at this location are computed from Eq. (9). In addition, the developed model explicitly gives the amplitudes of the downstream propagating acoustic waves exiting the injector, both in the coflow and in the fuel tube. The acoustic response of the injector can therefore be modeled in the LES by considering a non-reflecting injector inlet while imposing the incoming acoustic waves. The filtered quantities  $\tilde{u}$  and  $\tilde{p}$  are imposed using the NSCBC formulation described in Appendix A.

Other methods have been developed to account for the acoustic response of injector elements, such as the time domain impedance boundary condition (TDIBC) or the delayed-TDIBC. These methods typically prescribe the incoming characteristic wave as a function of the outgoing characteristic wave. The TDIBC approach can be solved via a variety of algorithms such as a state-space based formulation [42–44], an inverse discrete Fourier transform performed using the z-transform [45], or a convolution integral [46]. Delayed-TDIBC requires a tedious algorithm to approximate the reflection coefficient [47]. Compared to all these techniques, the approach employed in this paper is simpler, since the incoming characteristic wave is altered only using Eq. (11a). However, the current method is limited to configurations where the analytical solution of the acoustic field can be obtained.

### 3.3. Numerical set-up

We consider here the burner described in Section 2. The fuel and the oxidizer are methane and enriched air with 40%  $O_2$  by mass, respectively. The flow rates of the fuel and coflow streams are equal to  $\dot{m}_f = 0.164$  g/s and  $\dot{m}_c = 7.34$  g/s, respectively. Both streams are injected at a temperature of 293 K and at atmospheric pressure. In the following, we discuss the details relevant to the acoustic simulation and the LES of the reacting flow.

**Acoustic simulation** The block-structured mesh used to study the acoustics of the system consists of 330,000 hexahedral elements. Particular attention is given to ensure that the injector is well resolved. The fuel tube and post thickness wall have 34 and 4 elements across their width, respectively. A simulation on a finer mesh was also conducted to ensure that the velocity and pressure fluctuations inside the injector are converged. Subgrid stresses (SGS) are not modeled in the acoustic simulation.

The acoustic waves are prescribed from the two transverse boundaries, which model the speakers. The simulation is performed for the first PAN mode (i.e. at  $f = 360$  Hz) and therefore the waves injected at both ends are in phase, leading to a zero transverse velocity amplitude at the injector exit. The outlet is modeled as a partially reflecting Navier Stokes Characteristic Boundary Condition (NSCBC) [48] with a relaxation timescale of the order of 15 ms [49]. All other boundaries are modeled as slip, adiabatic walls. The complete chamber and injector are considered in this configuration. The honeycomb and metal sphere sections present in the experimental rig are assumed to have negligible acoustic resistance and are not considered in this geometry.

#### LES of the reacting flow

The computational domain considered for the LES is identical to the acoustic study, except for the injector geometry. The coflow annulus and fuel tube length are reduced to  $2D_f$  and their acoustic response is modeled (see Section 3.2). A block-structured mesh with 3.9 million hexahedral elements is used, with 40 and 8 elements across the fuel tube and post thickness wall, respectively.

Subgrid turbulence is modeled using the Vreman model [50]. The reaction chemistry for the methane/air combustion is described by the GRI3.0 mechanism, which consists of 53 species and 325 reactions. The mechanism is enhanced with the DLR  $OH^*$  sub-mechanism [51] to enable comparisons with experi-



**Table 1**  
Summary of LES configurations.

Case	Condition	Pressure amplitude $\Delta p$ [Pa]	Injector coupling
1	Unforced	0	No
2a	Moderate amplitude (w/o injector coupling)	300	No
2b	Moderate amplitude (with injector coupling)	300	Yes
3	High amplitude	450	Yes

mental data. The progress variable is defined as  $C = Y_{\text{CO}_2} + Y_{\text{CO}} + Y_{\text{H}_2\text{O}} + Y_{\text{H}_2}$  [52] and the stoichiometric mixture fraction is  $Z_{\text{st}} = 0.098$ . Constant turbulent Prandtl and Schmidt numbers of 0.7 are assumed for the scalar SGS model [53]. Due to the high Froude number,  $Fr = U_b^2/(gD_f) = 1.6 \times 10^4$  (with  $g$  the gravitational acceleration) buoyancy forces are not considered in the simulations.

Boundary conditions for the speakers and the injector inlet are prescribed using the NSCBC method described in Appendix A. While the former boundary only features incoming acoustic waves, turbulent inflow conditions are prescribed in the fuel tube. To this end, a synthetic turbulent flow is computed following the method proposed by Xie and Castro [54] with the modifications of Toubert and Sandham [55]. The mean and root mean square (RMS) profiles at an equivalent Reynolds number are used to define the fully developed pipe flow characteristics using an integral length scale of  $0.3D_f$ . The outlet is modeled by a non-reflecting NSCBC. A damping region, which relaxes the solution to a target, fully combusted, equilibrium state, is used in the exhaust section of the domain. This damping region prevents any thermodynamic or chemical inhomogeneities at the outlet that would lead to a spurious behavior with the non-reflecting locally one-dimensional and inviscid (LODI) boundary conditions. To this end, the formulation developed by Bogey et al. [56] is used, which is combined with a linear relaxation factor in the streamwise direction.

The chamber walls are treated as no-slip and adiabatic while the walls of the injector tube are modeled as no-slip and isothermal. The experiment did not include thermocouple measurements so literature data were used to estimate the wall temperature. Experimental non-premixed methane/air studies with similar flow velocities, rim thicknesses and rim material (i.e. copper) measured the lip to be at a maximum of 600 K [57,58], which was prescribed as the boundary wall temperature in the simulation. Altering the wall temperature by  $\pm 300$  K did not significantly change the flame stabilization and flame structure close to the boundaries.

Experimental [59] and numerical [60] studies have examined the structure for methane/air flames side-wall-quenching. They have found that 1) chemical wall effects are negligible at temperatures below 900 K and 2) there are negligible radical concentrations at 600 K. These results indicate that the flame quenches, leading to an absence of product species at the wall, which is consistent with the experiments of Kosaka et al. [61] at similar conditions. To account for these effects in the simulations, we therefore imposed a condition of  $\tilde{C} = 0$  at the injector tube wall, corresponding to a frozen chemistry [62]. The effects of pressure on chemistry are not taken into account given the small pressure fluctuations considered ( $< 1\%$ ).

Four different configurations were studied, as summarized in Table 1. These conditions correspond to experiments reported by Plascencia et al. [34]. An unforced flame is the baseline configuration (case 1). Two PAN configurations with moderate amplitude and pressure fluctuations  $\Delta p = 300$  Pa (cases 2a and 2b) were considered in order to examine the effect of the injector acoustic coupling on the lift-off. Finally, a high-amplitude case was considered (case 3). The excitation was performed at the first PAN mode in all cases, corresponding to a frequency of  $f = 360$  Hz and a Strouhal number  $St = fD_f/U_b = 0.0576$ .

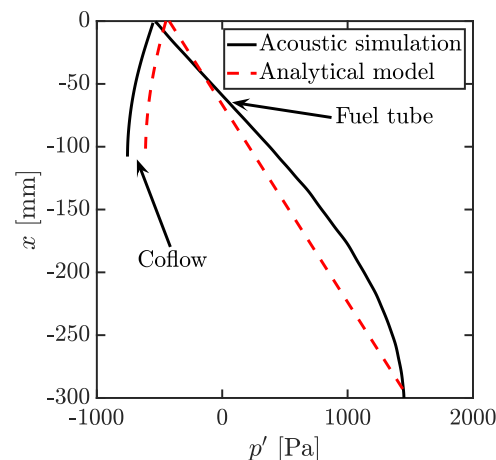


**Fig. 3.** Comparison of the pressure fluctuations inside the injector for case 2b obtained with the acoustic simulation and the analytical model.

## 4. Results

### 4.1. Acoustic simulation and modeling

To assess the analytical model for the inlet boundary conditions, we perform an acoustic simulation for case 2b at the first PAN mode and a forcing amplitude of  $\Delta p = 300$  Pa. In this simulation, the injector geometry is considered in its entirety.

Figure 3 shows comparisons of the pressure fluctuations inside the fuel tube and the coflow between the simulation and the model. Substantial pressure fluctuations are observed inside the injector and the interaction of the acoustic waves within the injector leads to pressure fluctuations that are much higher at the bottom of the fuel tube than inside the chamber. The good agreement between the simulation and analytical model suggests that the behavior of the acoustic waves described in Section 3.2 is physical.

Velocity fluctuations obtained at the exits of the coflow annulus and the fuel tube are shown in Fig. 4, as a function of the normalized time  $t_f = ft$ . The transverse velocity fluctuations are of the order of 0.01 m/s so only the streamwise component is discussed. The fuel tube velocity signal features an acoustic beating mode, resulting from the superposition of the forcing frequency and the first resonant frequency of the fuel tube  $f_1 = c/(4L_f) \simeq 280$  Hz. This result confirms that the exit of the tube acts as a reflecting interface for the acoustic waves and that losses are negligible, as assumed in the model and supported by the theory of Levine and Schwinger [39] that predicts a near-unity reflection coefficient for the frequency and tube diameter considered.

In contrast, the coflow signal is quasi-harmonic at the forcing frequency of  $f = 360$  Hz, showing that the open-end of the annulus is nearly non-reflecting. According to Levine and Schwinger [39], the reflection coefficient for a pipe of equivalent diameter should be 0.86. It is likely that the reflection coefficient in the acoustic simulation is lower than the theoretical value and we believe that the former approach is more reliable to establish that the coflow annulus can be approximated as a non-reflecting open-end.

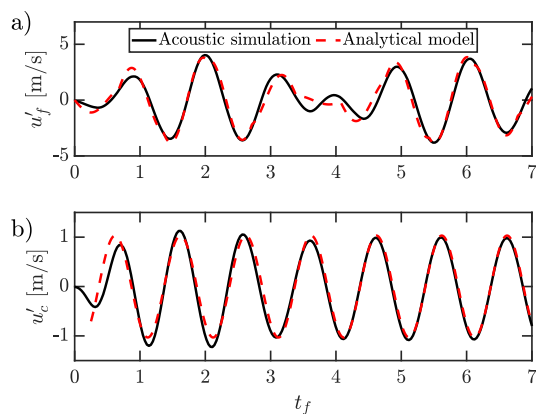


**Fig. 4.** Velocity fluctuations at the exit of a) the fuel tube and b) the coflow obtained with the acoustic simulations and the analytical model (Eq. (11a) and Eq. (8b)).

To further assess the analytical model, Eqs. (8b) and (11a) are compared to the simulation results in Fig. 4. Amplitude and phase are in good agreement for the coflow. In addition, the beating behavior in the fuel tube is well captured by the analytical model, especially when the velocity fluctuations are maximum. The discrepancy observed for  $t_f \leq 1$  in Fig. 4(b) represents the transient behavior of the simulation, which was initialized without any acoustic perturbations in the domain. Overall, these results show that the acoustic behavior in the fuel tube is well represented by linear acoustics with a perfectly reflecting open end and negligible losses. Furthermore, they illustrate that the acoustic waves can lead to strong variations in the mass flow rate, especially in the fuel tube.

#### 4.2. Qualitative comparison to experimental data

We proceed by analyzing the LES results and compare Schlieren images from the simulations with experimental data. The phase taken for comparison in the forced cases is established based on the lift-off height. The methodology used to post-process the LES results is described in Appendix B. Even though this comparison is mostly qualitative, it enables us to verify that the main flow and flame dynamics are captured by the LES. Comparisons of results for the cases 1, 2b and 3 are shown in Fig. 5.

Figure 5 (a) shows case 1, corresponding to the unforced configuration. The Schlieren images show the location of the flame, which widens as it is convected downstream. The development of the jet instability and the mixing is also apparent in the jet region. In addition, the flame remains anchored and stable. All these features are captured by the simulation.

In the moderately forced case 2b, shown in Fig. 5(b), the flame periodically lifts-off a few mm above the rim and exhibits a puff-like behavior. The small vortical structures present near the injector coalesce into larger ones and subsequently deform the flame, alternatively pushing it away or pulling it closer to the centerline. Even though the experimental results display smaller cellular regions in the downstream region, the main features are also present in the LES results. The high-amplitude case 3 is shown in Fig. 5(c). The flame is completely lifted, a few jet diameters above the rim. The puff-like structures are still present, but are smaller at the flame base compared to the lower amplitude forcing. The radial expansion of the flame is also more pronounced for this configuration. The LES results are again in good qualitative agreement with experimental observations.

To further assess the simulation results, Fig. 6 compares OH\* images from numerical and experimental data for the unforced and forced cases. An Abel transform of the OH\* mass fraction at the

$x - y$  centerplane obtained from the LES was performed. The experimental results show the average line-of-sight OH\* chemiluminescence imaging. The flame radial expansion and the chemiluminescence amplitude are well predicted by the LES, for both the unforced and for the forced cases. For the forced cases, the mean lift-off height is also well predicted. Overall, Figs. 5 and 6 show that the numerical and experimental results are in good agreement, indicating that the modeling approach and boundary conditions are well suited to predict the flame dynamics.

#### 4.3. Lift-off comparison to experimental data

We proceed by examining the lift-off predictions. Baillet and Demare [32], Demare and Baillet [33] have analyzed non-premixed combustion regimes and changes in lift-off height induced by longitudinal acoustic forcing at the fuel nozzle. For forcing frequencies comparable to our study, they showed that a forcing of sufficient amplitude leads to a flame which cannot stay anchored. This suggests that, in our configuration, the fuel tube forcing can lead to detachment of the flame. The analytical model provides quantitative results for the maximum velocity fluctuation amplitude at the fuel tube outlet  $u'_{f,max}$  (Eq. (11a)), which is shown in Fig. 7(a) as a function of the forcing frequency for  $\Delta p = 300$  Pa. When the forcing occurs close to the resonant frequency of the fuel tube (solid red lines),  $u'_{f,max}$  attains large values due to the acoustic energy build up. In contrast,  $u'_{f,max}$  is zero at the resonant frequency of the coflow (dashed blue lines). This can be explained by the zero pressure fluctuations at the coflow outlet. Therefore, the fuel tube is acoustically not excited, showing that the whole injector configuration needs to be considered to accurately describe the fuel flow rate fluctuations.

Unfortunately, velocity measurements were not performed in the experiments. To establish the minimum velocity fluctuations necessary to lift the flame, we calibrate the model with experimental results of the lift-off data. At  $f = 360$  Hz, the lift-off was observed at  $180 < \Delta p < 220$  Pa. The analytical model (Eq. (11a)) predicts  $u'_{lift} \simeq 4.5$  m/s, which is therefore used as condition for the flame to lift off. Knowing that  $u'_{f,max}$  is linearly dependent on the forcing amplitude  $\Delta p$ , one can therefore compute the required forcing amplitude to lift the flame as  $\Delta p_{lift} = u'_{lift} \Delta p / u'_{f,max}$ , which is shown in Fig. 7(b). In accordance with Fig. 7(a), only infinitesimal pressure perturbations are necessary to lift the flame at the resonant frequency of the fuel tube and lift-off cannot be achieved at the coflow resonant frequency. Experimental results are also shown for the second and third PAN frequencies i.e., at 775 Hz and 1150 Hz, and agree well with the analytical model.

Finally, the lift-off dynamics for the forced cases is analyzed. The flame location is tracked based on a threshold of the OH\* fields (shown in Fig. 6) equal to 20% of the maximum intensity. The line-of-sight OH\* chemiluminescence and the  $Y_{OH^*}$  Abel transforms are used for the experimental and numerical results, respectively. Instantaneous and phase-averaged results of the lift-off distance are reported in Fig. 8, both for the moderate (case 2) and high amplitude (case 3) forcing cases. The results with the injector coupling (case 2b and case 3, solid red lines) show an overall good agreement in the phase and peak values. Because the lift-off process is affected by turbulence in the fuel nozzle, there are however instantaneous differences. Phase-averaged results confirm the overall good agreement for phase and amplitude between the two signals, which only differ by a maximum of 0.5 mm and 1 mm for case 2b and case 3, respectively.

Figure 8 (a) (dashed line) also shows the instantaneous lift-off obtained when the injector coupling is not considered. In this configuration, the transverse acoustic waves diffract in the coflow injector but are not reflected back, leading to an under-prediction of

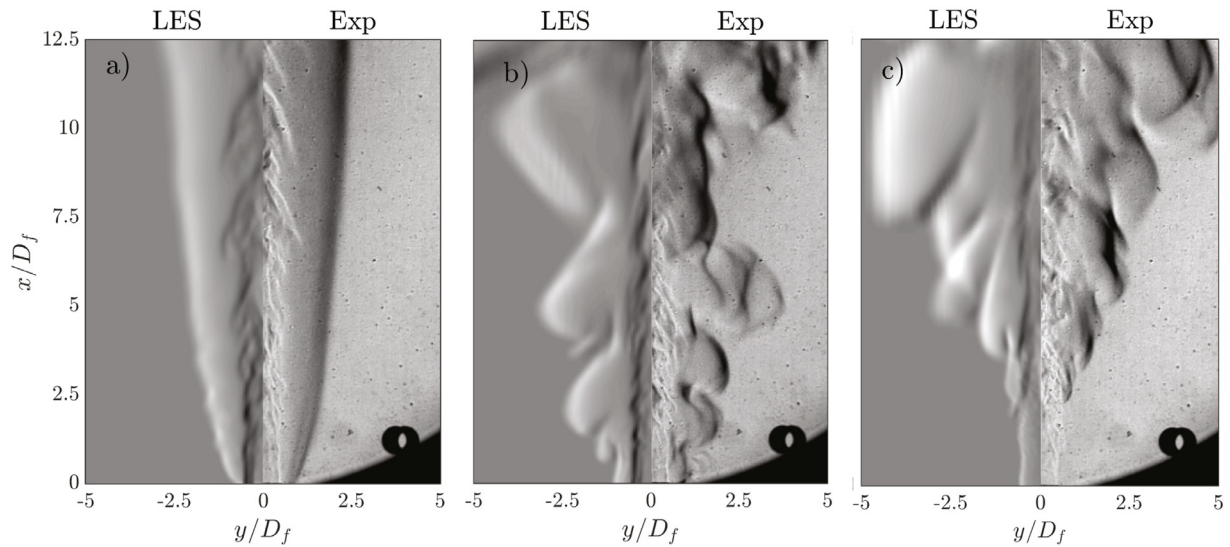


**Fig. 5.** Comparison between instantaneous numerical (left panels) and experimental (right panels) Schlieren images for a) the unforced case 1, b) the forced case 2b ( $\Delta p = 300$  Pa) and c) the forced case 3 ( $\Delta p = 450$  Pa).

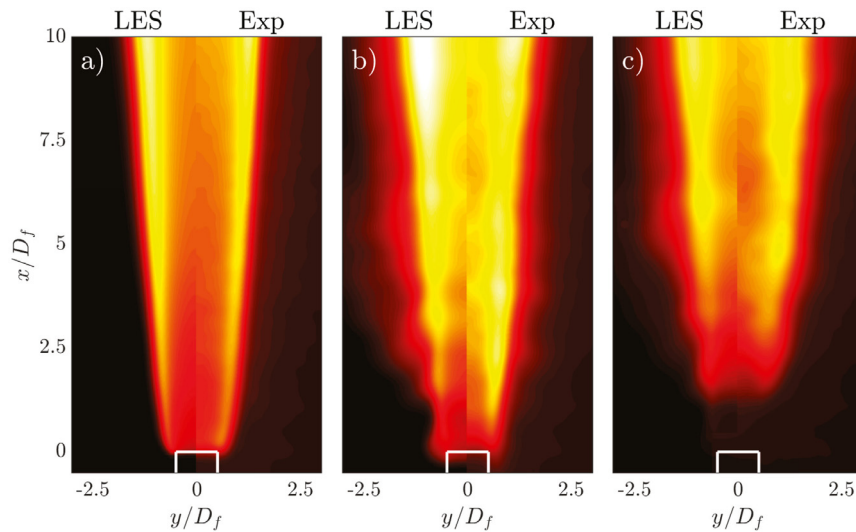


**Fig. 6.** Comparison between time-averaged numerical (left panels) and experimental (right panels) OH\* chemiluminescence imaging for a) the unforced case 1, b) the forced case 2b ( $\Delta p = 300$  Pa) and c) the forced case 3 ( $\Delta p = 450$  Pa). The injector is schematized by the white lines. OH\* is normalized with its maximum value.

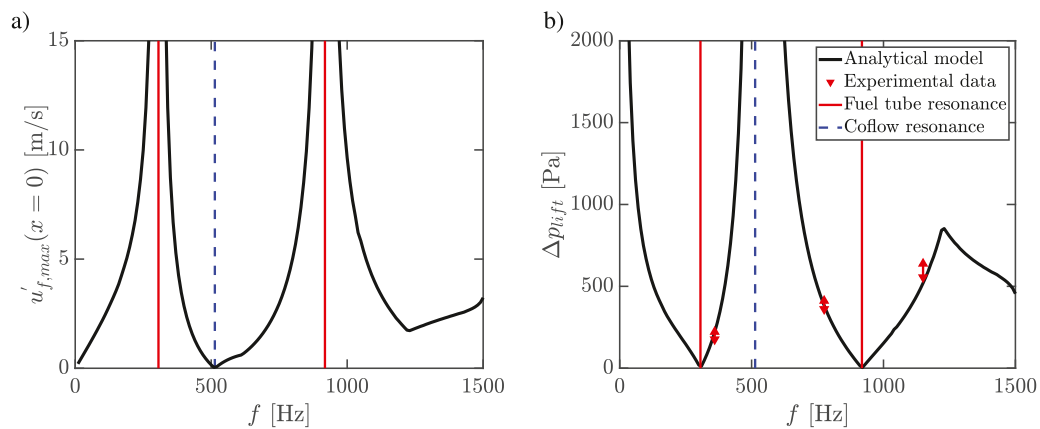


**Fig. 7.** Acoustic response at the fuel tube exit. The black line represents results from the analytical model showing a) the maximum  $u'_f$  amplitude at the fuel tube outlet for a forcing amplitude  $\Delta p = 300$  Pa and b) the minimum forcing amplitude necessary to lift-off the flame. The red markers represent the experimental results. (For interpretation of the references to colour in this figure legend, the reader is referred to the web version of this article.)

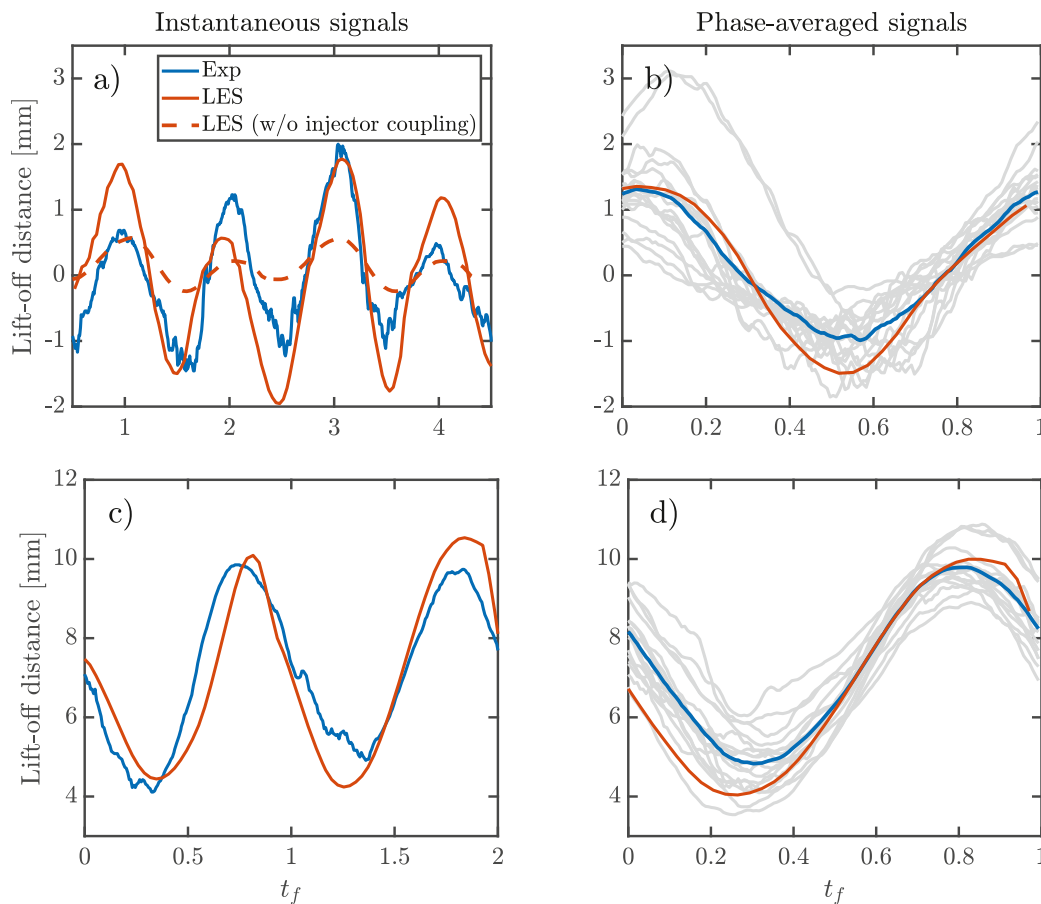


**Fig. 8.** Instantaneous (left column) and phase-averaged (right column) lift-off distance for (a-b) cases 2a and 2b and (c-d) case 3. The grey lines represent the instantaneous experimental data.

the streamwise velocity fluctuations at the injector exit. In turn, this leads to a substantial under-prediction of the lift-off oscillations. This result confirms the importance of the acoustic coupling of the injector to predict the lift-off dynamics of the flame.

Overall, we can draw two major conclusions from the unforced and forced lift-off comparisons. Firstly, it confirms that the modeling approach described in Section 3.1 is suited to predict the flame anchoring and lift-off dynamics. Secondly, the injector acoustic coupling must be considered to accurately predict the lift-off dynamics. This can be done by including the upstream injector geometry in the simulations or by modeling their effects on the velocity fluctuations, as performed in this study. The latter approach is computationally more efficient since the injector can extend spatially far upstream.

#### 4.4. Flame, flow and mixing dynamics

We proceed by examining the flame, flow, and mixing dynamics resulting from the acoustic forcing. We only consider the moderately forced flame (case 2b) since the results were qualitatively similar at a higher forcing amplitude. We start our analysis by discussing snapshots of the results over a forcing cycle in Fig. 9(a-e). The temperature field at the  $x - y$  centerplane displays puff-like characteristics. The isoline indicates the stoichiometric contour with  $Z_{st} = 0.098$  which is substantially corrugated by the surrounding flow field in the first ten jet diameters downstream of the inlet. Further downstream, these wrinkles are then weakened by diffusion. The regions with heat release rate larger than  $\dot{Q} = 5$  GW/m<sup>3</sup> are shown by the white isosurfaces and tend to be located

in the lower part of the flame. In order to examine the coupling between inlet fluctuations and heat release, we compare the temporal evolution of these isosurfaces with the traces of the spatially integrated heat release rate fluctuations ( $\dot{\Omega}'$ ) and the fuel mass flow rate, shown in Fig. 9(f). From panel (a) to (d), the fuel flow rate and heat release fluctuations transition from a minimum to a maximum value, illustrating the causal relationship between inflow and heat release rate fluctuations. Strong mass flow and heat release rate oscillations, of the order of 40% and 10% of their nominal values, respectively, are observed. In the following, we analyze the physical mechanisms responsible for this coupling.

To identify the main flame and flow features, Spectral Proper Orthogonal Decomposition (SPOD) is employed [63]. This method identifies spatially orthogonal modes at particular frequencies, based on a cross-correlation tensor of realizations of the temporal Fourier transform. A full description of the methodology, which has been successfully applied to non-reacting [64] and reacting [65,66] flows, can be found in [63]. Figure 10(a) shows the dominant SPOD modes of the temperature and transverse velocity fields at the forcing frequency of 360 Hz. An instantaneous isoline of the stoichiometric isosurface is shown by the black line to visualize the flow effect on the flame. The temperature mode is first discussed. An elongated structure is identified in the jet region, which is caused by the acoustic forcing in the fuel tube. Another main flame feature is located near the inflow on the outer edge of the fuel tube, which represents the streamwise oscillations of the flame base caused by fluctuations in the coflow longitudinal velocity. Large transverse velocity fluctuations are also noted in this region, which introduce the temperature oscillations seen in the left



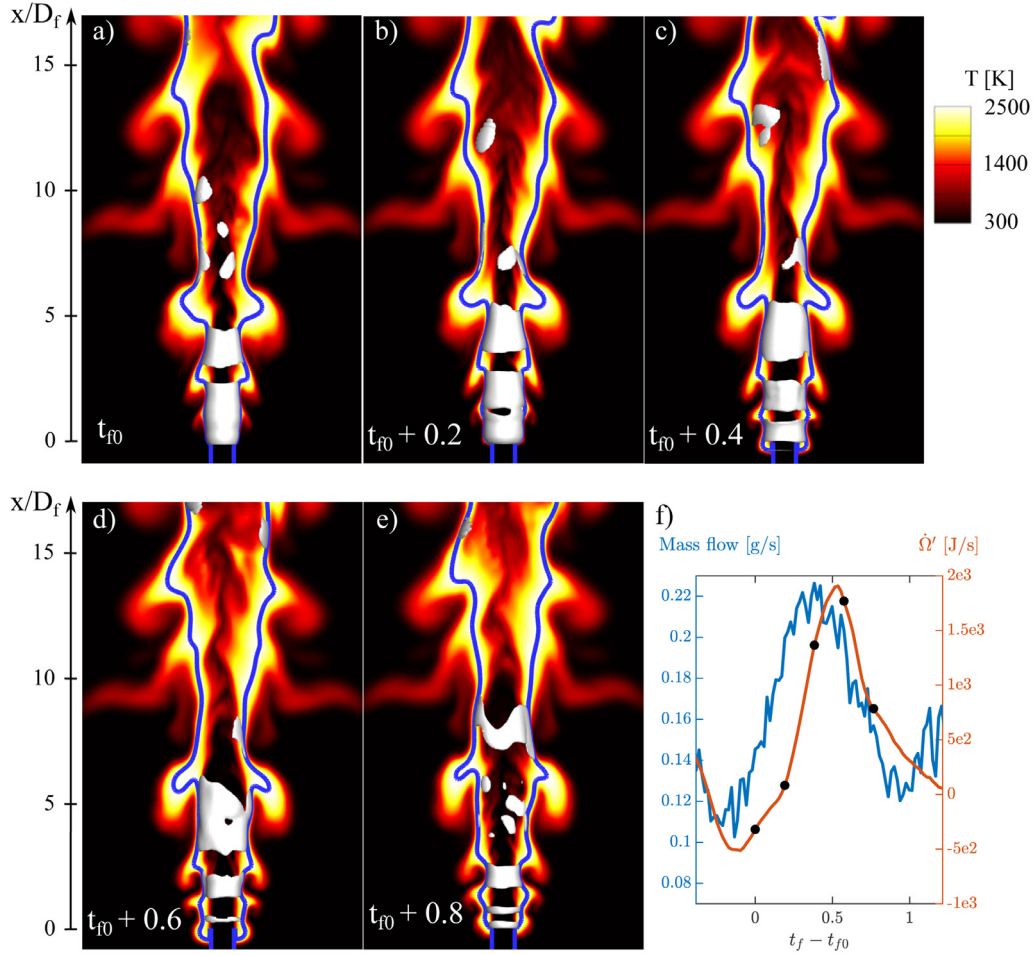


**Fig. 9.** a-e) Evolution of the flame on the  $x - y$  centerplane over a forcing cycle. The colorplots represent the temperature field, the isolines show  $Z_{st} = 0.098$  and the iso-surfaces show  $\dot{Q} = 5$  GW/m<sup>2</sup>. f) Corresponding fuel flow rate and integrated heat release rate. The scatter points represent the instants shown in panels a-e).

panel of Fig. 10(a). These velocity modulations, however, do not alter significantly the stoichiometric surface and are not identified for  $x/D_f > 3$ . It is noted that no vortices or flame motion were observed in the unforced case 1. Therefore, it can be concluded that the structures discussed here are caused by the longitudinal acoustic forcing.

Figure 10 (b-c) display the dominant SPOD mode at the first and second subharmonics, respectively, showing the persistence of the temperature and the velocity fluctuations for  $x/D_f > 3$ . The streamwise growth and decay of these structures, as well as their downstream shift for lower frequencies, are indicative of a transfer of energy to lower subharmonics. This is likely the result of a lower convective velocity and vortex merging, which was also observed by Kim et al. [25] in their acoustically forced H<sub>2</sub>/air non-premixed coaxial flames. These vortices at subharmonic frequencies corrugate the flame in the downstream region, resulting in cusp-like shapes and large transverse fluctuations of the stoichiometric surface. Even if the longitudinal forcing occurs at a frequency much higher than the natural unstable mode (which is of the order of 10 Hz for this case [67]), the stoichiometric surface is still corrugated, albeit at sub-harmonic frequencies.

The effects of the fuel tube forcing are investigated next. A key quantity in non-premixed flames is the scalar dissipation rate, which represents the local mixing, and affects the flame structure and heat release rate. It is computed as  $\chi = 2D_T|\nabla Z|^2$ , where the thermal diffusion coefficient  $D_T$  is evaluated assuming a Prandtl number equal to  $Pr = 0.7$ . Figure 11 shows consecutive

snapshots of the  $\chi$ -field, as well as the streamwise velocity isolines  $u = \bar{u}(x = 0, y = 0) = 28$  m/s, which enables visualizing the forcing phase. As the inlet flow rate increases, the jet core expands radially due to the increased streamwise velocity. This results in an increase in the scalar dissipation rate further away from the centerline. This is particularly evident at  $t_f = 0.4$ , where large  $\chi$ -values are observed to expand radially around  $x/D_f = 3$ .

These results indicate a causal relation between the fuel flow rate  $\dot{m}$  and the radial location  $\zeta$  at which the scalar dissipation rate reaches its maximum. To estimate how far downstream the flow forcing impacts the mixing, a normalized cross-correlation  $R_{m\zeta, norm}$  is computed for a range of streamwise locations as  $R_{m\zeta}(x, \tau) / \sqrt{R_{mm}(x, 0)R_{\zeta\zeta}(x, 0)}$ , where  $R_{m\zeta}(x, \tau)$  denotes the cross-correlation coefficient between  $\dot{m}$  and  $\zeta$  with a time delay  $\tau$ . Figure 12 shows the maximum cross-correlation between the two signals and the time delay  $\tau$  at which it was obtained. The cross-correlation exceeds 0.5 up to  $x/D_f = 10$  and decreases significantly further downstream, showing that the jet acoustic forcing only impacts the mixing in the lower part of the flame. The time delay, which is less than a millisecond, follows a linear behavior and illustrates the time required for the inflow perturbations to be convected downstream.

To analyze the effect of the flow and flame dynamics on the heat release rate response, Fig. 13 shows the joint probability density functions (PDFs) between several quantities at the stoichiometric surface. The conditional mean and RMS are shown by the dashed white and red lines, respectively. Figure 13(a) shows the

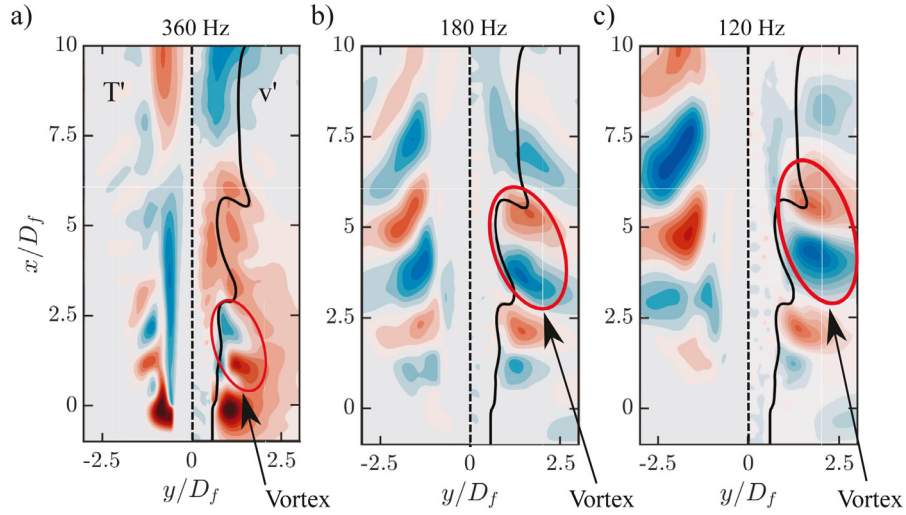


**Fig. 10.** Dominant SPOD modes for the temperature (left panels) and the transverse velocity (right panels) at a) the forcing frequency of 360 Hz, b) the first subharmonic (180 Hz) and c) the second subharmonic (120 Hz). The black isoline represents an instantaneous stoichiometric surface. The colorscales range from  $\pm 1000$  K and  $\pm 1.5$  m/s for the temperature and velocity, respectively.

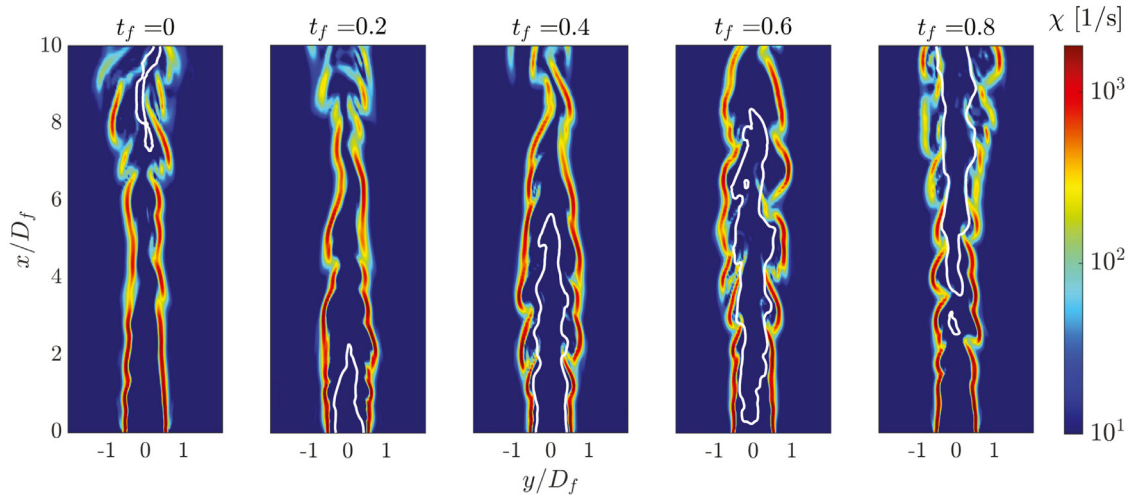


**Fig. 11.** Snapshots of the scalar dissipation field  $\chi$  and isoline of  $u = 28$  m/s at the  $x - y$  centerplane.

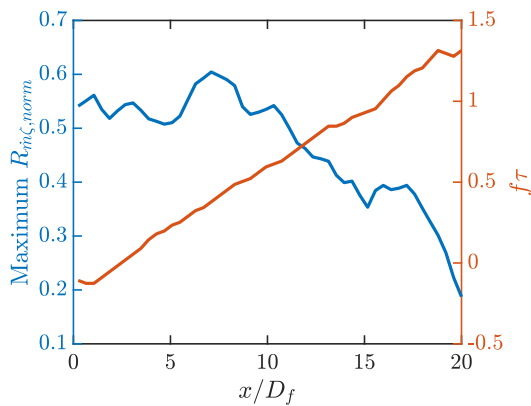


**Fig. 12.** Maximum normalized cross-correlation  $R_{\eta\zeta, norm}$  between the fuel flow rate and the radial position of maximum  $\chi$ , with corresponding time delay  $\tau$ .

joint PDF of the radial position of the stoichiometric surface and the scalar dissipation rate. The strong and monotonous increase in  $\chi$  as the flame moves closer to the centerline can be explained

by the higher radial gradient of the mixture fraction. Interestingly, the conditional RMS also increases substantially when the flame is closer to the centerline, especially for  $r/D_f < 1.5$ . The jet pulsation and subsequent radial expansion of the scalar dissipation rate field, shown in Fig. 11, provide an explanation for the increased fluctuations; when the stoichiometric surface is brought close enough to the centerline by the outer vortices, the mixing at the stoichiometric surface is periodically enhanced by the fuel tube forcing.

These results have direct implications on the local heat release rate, as illustrated by the joint PDF of  $\chi$  and  $\dot{Q}$  in Fig. 13(b). The mean and RMS of the heat release rate have a monotonous and quasi-linear dependence on  $\chi$ , consistent with the steady laminar flamelet theory [68]. Figure 13(c) shows the joint PDF of the radial position of the stoichiometric surface and the integrated heat release rate in the  $y-z$  plane. This figure illustrates the implication of this dependency; the flame will exhibit significantly larger heat release rate fluctuations when the stoichiometric surface is closer to the centerline.

It is important to note that two different mechanisms are necessary to obtain the behavior described in this section: 1) a transverse deformation of the stoichiometric surface by large vortices in the shear layer and 2) a jet forcing to enhance the mixing.

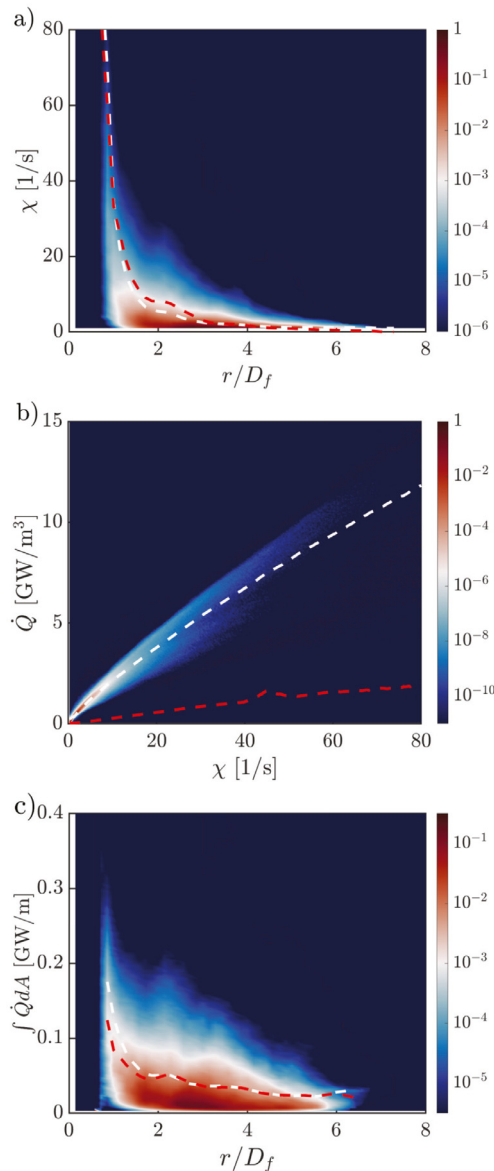


**Fig. 13.** Joint PDFs at the stoichiometric surface of a) the scalar dissipation rate  $\chi$  and the radial position  $r$ , b) the heat release rate  $\dot{Q}$  and  $\chi$ , and c) the integrated  $\dot{Q}$  in the  $y-z$  plane and  $r$ . The conditional mean and RMS are represented by the white and red dashed lines, respectively. (For interpretation of the references to colour in this figure legend, the reader is referred to the web version of this article.)

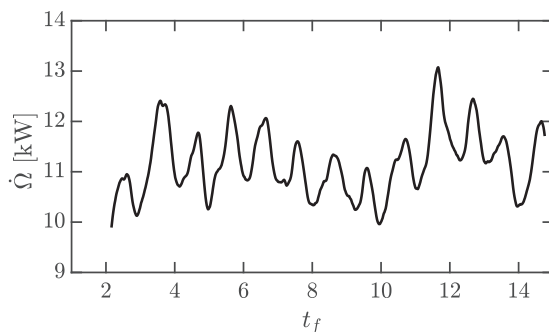


**Fig. 14.** Temporal evolution of volume integrated heat release rate.

This comes about in this configuration because the coflow annulus and the fuel tube introduce significant streamwise velocity fluctuations due to their acoustic response. As a result, substantial heat release rate oscillations were observed in the lower part of the flame. These fluctuations are also noticeable in the temporal evolution of the volume integrated heat release rate. Figure 14 demonstrates that the physical mechanisms described in this section lead to large fluctuations in heat release, of the order of 10% of the mean value. The positive heat release rate fluctuations are caused by the jet forcing, which enhances periodically the mixing at the forced frequency.

## 5. Conclusions

A turbulent non-premixed methane/air flame under a transverse acoustic mode was studied to understand the acoustic and flow mechanisms affecting the flame response. The flame was subjected to a standing pressure anti-node wave, where pressure oscillations are maximum at the centerline. Using this configuration, we studied two important aspects related to transverse combustion instabilities: the acoustic response of the injector and the flame/flow coupling mechanisms. From this study, the following conclusions were drawn:

- Acoustic simulations revealed that transverse acoustic modes introduce strong longitudinal velocity perturbations in the injector, both in the coflow and in the fuel jet. An analytical model was developed to predict the acoustic fluctuations in the injector, showing good agreement with simulation results.
- LES were performed using the analytical model for the inlet boundary conditions, and were compared to experimental measurements. The puff-like flame dynamics arising from the longitudinal forcing was captured in the LES and the lift-off dynamics was in good agreement with experimental data. It was shown that the injector acoustic coupling was the main mechanism for the transverse acoustic mode to affect the flame and must be considered to accurately predict the flame lift-off.
- Further analysis of the flow, mixing and flame processes revealed the flame response mechanisms. Vortices in the outer shear layer arising from the coflow forcing corrugated the flame in the near-nozzle region. Simultaneously, the jet forcing enhanced the mixing at greater radial locations. The combination of these two mechanisms was shown to periodically increase the heat release rate where the flame was close enough to the centerline. Hence, the longitudinal fluctuations in the coflow and the jet played complementary roles leading to substantial heat release rate oscillations in the near inflow region.

This work supports the hypothesis that strong acoustic/flame coupling can be present in non-premixed systems when the gaseous fuel and oxidizers injectors are longitudinally excited by transverse acoustic waves. Further work is needed to establish if the mechanisms discussed in this paper can lead to combustion instabilities in the studied configuration and different geometries, such as shear-coaxial flames.

## Declaration of Competing Interest

The authors declare that they have no known competing financial interests or personal relationships that could have appeared to influence the work reported in this paper.

## Acknowledgments

Financial support through the Air Force Research Laboratory (award # RAPF1-0000001326), the Air Force Office for Scientific



Research (award # FA9550-21-1-0077) and the Ohio Aerospace Institute is gratefully acknowledged. The computational resources supporting this work are provided by the National Energy Research Scientific Computing Center (NERSC). The help of D. Talley from AFRL in the analysis of the results is also kindly acknowledged.

## Supplementary material

Supplementary material associated with this article can be found, in the online version, at doi:[10.1016/j.combustflame.2022.112330](https://doi.org/10.1016/j.combustflame.2022.112330).

## References

- [1] *Combustion instabilities in gas turbine engines: operational experience, fundamental mechanisms and modeling*, T. Liewu, V. Yang (Eds.), American Institute of Aeronautics and Astronautics, 2005.
- [2] P. Wolf, G. Staffelbach, L. Gicquel, J.D. Müller, T. Poinot, Acoustic and large eddy simulation studies of azimuthal modes in annular combustion chambers, *Combust. Flame* 159 (11) (2012) 3398–3413, doi:[10.1016/j.combustflame.2012.06.01](https://doi.org/10.1016/j.combustflame.2012.06.01).
- [3] K. Priour, D. Durox, T. Schuller, S. Candel, A hysteresis phenomenon leading to spinning or standing azimuthal instabilities in an annular combustor, *Combust. Flame* 175 (2017) 283–291, doi:[10.1016/j.combustflame.2016.05.021](https://doi.org/10.1016/j.combustflame.2016.05.021).
- [4] D. Rouwenhorst, J. Hermann, W. Polifke, Online monitoring of thermoacoustic eigenmodes in annular combustion systems based on a state-space model, *J. Eng. Gas Turb. Power* 139 (2) (2017) 021502, doi:[10.1115/1.4034260](https://doi.org/10.1115/1.4034260).
- [5] N.A. Worth, J.R. Dawson, Self-excited circumferential instabilities in a model annular gas turbine combustor: global flame dynamics, *Proc. Combust. Inst.* 34 (2) (2013) 3127–3134, doi:[10.1016/j.proci.2012.05.061](https://doi.org/10.1016/j.proci.2012.05.061).
- [6] G. Vignat, D. Durox, A. Renaud, S. Candel, High amplitude combustion instabilities in an annular combustor inducing pressure field deformation and flame blow-off, *J. Eng. Gas Turb. Power* 142 (1) (2020) GTP–19–1629, doi:[10.1115/1.5020199](https://doi.org/10.1115/1.5020199).
- [7] A.M.A. Rocha, J.A. Carvalho, P.T. Lacava, Gas concentration and temperature in acoustically excited Delft turbulent jet flames, *Fuel* 87 (15–16) (2008) 3433–3444, doi:[10.1016/j.fuel.2008.01.010](https://doi.org/10.1016/j.fuel.2008.01.010).
- [8] M.P. Juniper, L.K.B. Li, J.W. Nichols, Forcing of self-excited round jet diffusion flames, *Proc. Combust. Inst.* 32 (2009) 1191–1198, doi:[10.1016/j.proci.2008.05.065](https://doi.org/10.1016/j.proci.2008.05.065).
- [9] J. O'Connor, Visualization of shear layer dynamics in a transversely forced flow and flame, *J. Propul. Power* 31 (4) (2015) 1127–1136, doi:[10.2514/6.2015-1136](https://doi.org/10.2514/6.2015-1136).
- [10] N.A. Worth, J.R. Dawson, J.A. Sidey, E. Mastorakos, Azimuthally forced flames in an annular combustor, *Proc. Combust. Inst.* 36 (3) (2017) 3783–3790, doi:[10.1016/j.proci.2016.06.107](https://doi.org/10.1016/j.proci.2016.06.107).
- [11] N. Purwar, M. Haeringer, B. Schuermans, W. Polifke, Flame response to transverse velocity excitation leading to frequency doubling and modal coupling, *Combust. Flame* 230 (2021) 111412, doi:[10.1016/j.combustflame.2021.111412](https://doi.org/10.1016/j.combustflame.2021.111412).
- [12] J. O'Connor, V. Acharya, T. Liewu, Transverse combustion instabilities: acoustic, fluid mechanic, and flame processes, *Prog. Energy Combust. Sci.* 49 (2015) 1–39, doi:[10.1016/j.peccs.2015.01.001](https://doi.org/10.1016/j.peccs.2015.01.001).
- [13] A. Urbano, L. Selle, Driving and damping mechanisms for transverse combustion instabilities in liquid rocket engines, *J. Fluid Mech.* 820 (2017) R2, doi:[10.1017/jfm.2017.227](https://doi.org/10.1017/jfm.2017.227).
- [14] U. Krüger, J. Hüren, S. Hoffmann, W. Krebs, D. Bohn, Prediction of thermoacoustic instabilities with focus on the dynamic flame behavior for the 3a-series gas turbine of siemens KWU, *Turbo Expo: Power for Land, Sea, and Air*, 78590, 1999. V002T02A016.
- [15] S. Gröning, J.S. Hardi, D. Suslov, M. Oschwald, Injector-driven combustion instabilities in a hydrogen/oxygen rocket combustor, *J. Propul. Power* 32 (2016) 560–573.
- [16] W. Armbruster, J.S. Hardi, D. Suslov, M. Oschwald, Injector-driven flame dynamics in a high-pressure multi-element oxygen–hydrogen rocket thrust chamber, *J. Propul. Power* 35 (2019) 632–644.
- [17] W. Krebs, G. Walz, S. Hoffmann, Thermoacoustic analysis of annular combustor, *AIAA Pap.* (1999). 1999–1971.
- [18] S.R. Stow, A.P. Dowling, Thermoacoustic oscillations in an annular combustor, *Turbo Expo: Power for Land, Sea, and Air*, 78514, 2001. V002T02A004.
- [19] U. Krüger, J. Hüren, S. Hoffmann, W. Krebs, P. Flohr, D. Bohn, Prediction and measurement of thermoacoustic improvements in gas turbines with annular combustion systems, *J. Eng. Gas Turb. Power* 123 (2001) 557–566.
- [20] J. Blimbaum, M. Zanchetta, T. Akin, V. Acharya, J. O'Connor, D. Noble, T. Liewu, Transverse to longitudinal acoustic coupling processes in annular combustion chambers, *Int. J. Spray Combust.* 4 (2012) 275–298, doi:[10.1260/1756-8277.4.4.275](https://doi.org/10.1260/1756-8277.4.4.275).
- [21] C.C. Hantschk, D. Vortmeyer, Numerical simulation of self-excited combustion oscillations in a non-premixed burner, *Combust. Sci. Technol.* 174 (1) (2002) 189–204, doi:[10.1080/0713712912](https://doi.org/10.1080/0713712912).
- [22] S.R. Chakravarthy, O.J. Shreenivasan, B. Boehm, A. Dreizler, J. Janicka, Experimental characterization of onset of acoustic instability in a nonpremixed half-dump combustor, *J. Acoust. Soc. Am.* 122 (1) (2007) 120–127, doi:[10.1121/1.2741374](https://doi.org/10.1121/1.2741374).
- [23] Y.C. Yu, S.M. Koeglmeier, J.C. Sisco, W.E. Anderson, Combustion instability of gaseous fuels in a continuously variable resonance chamber (CVRC), *AIAA Pap.* (2008) 2008–4657, doi:[10.2514/6.2008-4657](https://doi.org/10.2514/6.2008-4657).
- [24] S. Srinivasan, R. Ranjan, S. Menon, Flame dynamics during combustion instability in a high-pressure, shear-coaxial injector combustor, *Flow Turbul. Combust.* 94 (2015) 237–262, doi:[10.1007/s10494-014-9569-x](https://doi.org/10.1007/s10494-014-9569-x).
- [25] M. Kim, Y. Choi, J. Oh, Y. Yoon, Flame-vortex interaction and mixing behaviors of turbulent non-premixed jet flames under acoustic forcing, *Combust. Flame* 156 (12) (2009) 2252–2263, doi:[10.1016/j.combustflame.2009.08.004](https://doi.org/10.1016/j.combustflame.2009.08.004).
- [26] H. Zhou, S. Meng, C. Tao, Z. Liu, Study of burner geometry effects on non-premixed flame response under acoustic excitation, *J. Low Freq. Noise Vib. Act. Control* 38 (1) (2019) 3–17, doi:[10.1177/1461348418815411](https://doi.org/10.1177/1461348418815411).
- [27] N. Magina, D.H. Shin, V. Acharya, T. Liewu, Response of non-premixed flames to bulk flow perturbations, *Proc. Combust. Inst.* 34 (1) (2013) 963–971, doi:[10.1016/j.proci.2012.06.155](https://doi.org/10.1016/j.proci.2012.06.155).
- [28] N. Magina, V. Acharya, T. Liewu, Forced response of laminar non-premixed jet flames, *Prog. Energy Combust. Sci.* 70 (2019) 89–118, doi:[10.1016/j.peccs.2018.08.001](https://doi.org/10.1016/j.peccs.2018.08.001).
- [29] J.A. Lovett, S.R. Turns, The structure of pulsed turbulent nonpremixed jet flames, *Combust. Sci. Technol.* 94 (1993) 193–217, doi:[10.1080/00102209308935310](https://doi.org/10.1080/00102209308935310).
- [30] J. Min, F. Baillot, Experimental investigation of the flame extinction processes of nonpremixed methane flames inside an air coflow diluted with CO<sub>2</sub>, N<sub>2</sub>, or Ar, *Combust. Flame* 159 (2012) 3502–3517.
- [31] M. Marin, F. Baillot, Experimental study of the lifting characteristics of the leading-edge of an attached non-premixed jet-flame: air-side or fuel-side dilution, *Combust. Flame* 171 (2016) 264–280, doi:[10.1016/j.combustflame.2016.05.025](https://doi.org/10.1016/j.combustflame.2016.05.025).
- [32] F. Baillot, D. Demare, Responses of a lifted non-premixed flame to acoustic forcing, Part 2, *Combust. Sci. Technol.* 179 (5) (2007) 905–932, doi:[10.1080/00102200600713252](https://doi.org/10.1080/00102200600713252).
- [33] D. Demare, F. Baillot, Acoustic enhancement of combustion in lifted non-premixed jet flames, *Combust. Flame* 139 (4) (2004) 312–328, doi:[10.1016/j.combustflame.2004.09.004](https://doi.org/10.1016/j.combustflame.2004.09.004).
- [34] M. Plascencia, M. Roa, A. Karagozian, D.G. Talley, Turbulent nonpremixed jet flames under transverse acoustic forcing, *AIAA Pap.* (2020) 2020–3805, doi:[10.2514/6.2020-3805](https://doi.org/10.2514/6.2020-3805).
- [35] Y. Khalighi, F. Ham, J. Nichols, S. Lele, P. Moin, Unstructured large eddy simulation for prediction of noise issued from turbulent jets in various configurations, *AIAA Pap.* (2011) 2011–2886, doi:[10.2514/6.2011-2886](https://doi.org/10.2514/6.2011-2886).
- [36] P.C. Ma, Y. Lv, M. Ihme, An entropy-stable hybrid scheme for simulations of transcritical real-fluid flows, *J. Comput. Phys.* 340 (2017) 330–357, doi:[10.1016/j.jcp.2017.03.022](https://doi.org/10.1016/j.jcp.2017.03.022).
- [37] C.D. Pierce, P. Moin, Progress-variable approach for large-eddy simulation of non-premixed turbulent combustion, *J. Fluid Mech.* 504 (2004) 73–97, doi:[10.1017/S0022112004008213](https://doi.org/10.1017/S0022112004008213).
- [38] M. Ihme, C.M. Cha, H. Pitsch, Prediction of local extinction and re-ignition effects in non-premixed turbulent combustion using a flamelet/progress variable approach, *Proc. Combust. Inst.* 30 (2005) 793–800, doi:[10.1016/j.proci.2004.08.260](https://doi.org/10.1016/j.proci.2004.08.260).
- [39] H. Levine, J. Schwinger, On the radiation of sound from an unflanged circular pipe, *Phys. Rev.* 73 (4) (1947) 383–406.
- [40] L. Van Wijngaarden, On the oscillations near and at resonance in open pipes, *J. Eng. Math.* 2 (3) (1968) 225–240, doi:[10.1007/BF01535773](https://doi.org/10.1007/BF01535773).
- [41] S.W. Rienstra, A. Hirschberg, *An introduction to acoustics*, Eindhoven University of Technology, 2004.
- [42] S. Jaensch, C. Sovardi, W. Polifke, On the robust, flexible and consistent implementation of time domain impedance boundary conditions for compressible flow simulations, *J. Comput. Phys.* 314 (2016) 145–159, doi:[10.1016/j.jcp.2016.03.010](https://doi.org/10.1016/j.jcp.2016.03.010).
- [43] S. Jaensch, M. Merk, E. Gopalakrishnan, S. Bomberg, T. Emmert, R. Sujith, W. Polifke, Hybrid CFD/low-order modeling of nonlinear thermoacoustic oscillations, *Proc. Combust. Inst.* 36 (2017) 3827–3834.
- [44] P. Tudosco, R. Ranjan, S. Menon, S. Jaensch, W. Polifke, Application of the time-domain impedance boundary condition to large-eddy simulation of combustion instability in a shear-coaxial high pressure combustor, *Flow Turbul. Combust.* 99 (2017) 185–207.
- [45] R. Kaess, A. Huber, W. Polifke, A time-domain impedance boundary condition for compressible turbulent flow, *AIAA Pap.* (2008) 2008–2921.
- [46] K.-Y. Fung, H. Ju, Time-domain impedance boundary conditions for computational acoustics and aeroacoustics, *Int. J. Comput. Fluid D.* 18 (2004) 503–511.
- [47] Q. Douasbin, C. Scalo, L. Selle, T. Poinot, Delayed-time domain impedance boundary conditions (D-TDIBC), *J. Comput. Phys.* 371 (2018) 50–66.
- [48] T. Poinot, S.K. Lele, Boundary conditions for direct simulations of compressible viscous flows, *J. Comput. Phys.* 101 (1) (1992) 104–129.
- [49] L. Selle, F. Nicoud, T. Poinot, Actual impedance of nonreflecting boundary conditions: implications for computation of resonators, *AIAA J.* 42 (2004) 958–964.
- [50] A.W. Vreman, J.A. Van Oijen, L.P.H. De Goey, R.J.M. Bastiaans, Subgrid scale modeling in large-eddy simulation of turbulent combustion using premixed flamelet chemistry, *Flow Turbul. Combust.* 82 (4) (2009) 511–535, doi:[10.1007/s10494-008-9159-x](https://doi.org/10.1007/s10494-008-9159-x).
- [51] T. Kathrotia, *Reaction kinetics modeling of OH\*, CH\*, and C2\* chemiluminescence*, Ruprecht Karl University of Heidelberg, 2011 Ph.D. thesis.
- [52] M. Ihme, L. Shunn, J. Zhang, Regularization of reaction progress variable for application to flamelet-based combustion models, *J. Comput. Phys.* 231 (23) (2012) 7715–7721, doi:[10.1016/j.jcp.2012.06.029](https://doi.org/10.1016/j.jcp.2012.06.029).



- [53] C. Pantano, Direct simulation of non-premixed flame extinction in a methane - air jet with reduced chemistry, *J. Fluid Mech.* 514 (2004) 231–270, doi:[10.1017/S0022112004000266](https://doi.org/10.1017/S0022112004000266).
- [54] Z.T. Xie, I.P. Castro, Efficient generation of inflow conditions for large eddy simulation of street-scale flows, *Flow Turbul. Combust.* 81 (3) (2008) 449–470, doi:[10.1007/s10494-008-9151-5](https://doi.org/10.1007/s10494-008-9151-5).
- [55] E. Touber, N.D. Sandham, Large-eddy simulation of low-frequency unsteadiness in a turbulent shock-induced separation bubble, *Theor. Comp. Fluid Dyn.* 23 (2) (2009) 79–107, doi:[10.1007/s00162-009-0103-z](https://doi.org/10.1007/s00162-009-0103-z).
- [56] C. Bogey, C. Bailly, D. Juve, Numerical simulation of sound generated by vortex pairing in a mixing layer, *AIAA J.* 38 (12) (2000) 2210–2218, doi:[10.2514/2.906](https://doi.org/10.2514/2.906).
- [57] S. Lamige, K.M. Lyons, C. Galizzi, F. André, M. Kühni, D. Escudié, Burner lip temperature and stabilization of a non-premixed jet flame, *Exp. Therm. Fluid Sci.* 56 (2014) 45–52, doi:[10.1016/j.expthermflusci.2013.11.008](https://doi.org/10.1016/j.expthermflusci.2013.11.008).
- [58] T. Guiberti, W. Boyette, A. Masri, W. Roberts, Detachment mechanisms of turbulent non-premixed jet flames at atmospheric and elevated pressures, *Combust. Flame* 202 (2019) 219–227, doi:[10.1016/j.combustflame.2019.01.019](https://doi.org/10.1016/j.combustflame.2019.01.019).
- [59] Y. Saiki, Y. Fan, Y. Suzuki, Radical quenching of metal wall surface in a methane-air premixed flame, *Combust. Flame* 162 (10) (2015) 4036–4045, doi:[10.1016/j.combustflame.2015.07.043](https://doi.org/10.1016/j.combustflame.2015.07.043).
- [60] J. Andrae, P. Björnbohm, L. Edsberg, Numerical studies of wall effects with laminar methane flames, *Combust. Flame* 128 (1–2) (2002) 165–180, doi:[10.1016/S0010-2180\(01\)00342-X](https://doi.org/10.1016/S0010-2180(01)00342-X).
- [61] H. Kosaka, F. Zentgraf, A. Scholtissek, L. Bischoff, T. Häber, R. Suntz, B. Albert, C. Hasse, A. Dreizler, Wall heat fluxes and CO formation/oxidation during laminar and turbulent side-wall quenching of methane and DME flames, *Int. J. Heat Fluid Flow* 70 (2018) 181–192, doi:[10.1016/j.ijheatfluidflow.2018.01.009](https://doi.org/10.1016/j.ijheatfluidflow.2018.01.009).
- [62] N. Perakis, O.J. Haidn, M. Ihme, Investigation of co recombination in the boundary layer of CH<sub>4</sub>/O<sub>2</sub> rocket engines, *Proc. Combust. Inst.* 38 (4) (2021) 6403–6411, doi:[10.1016/j.proci.2020.07.080](https://doi.org/10.1016/j.proci.2020.07.080) 1540–7489.
- [63] O.T. Schmidt, T. Colonius, Guide to spectral proper orthogonal decomposition, *AIAA J.* 58 (3) (2020) 1023–1033, doi:[10.2514/1.j058809](https://doi.org/10.2514/1.j058809).
- [64] O.T. Schmidt, A. Towne, G. Rigas, T. Colonius, G.A. Brès, Spectral analysis of jet turbulence, *J. Fluid Mech.* 855 (2018) 953–982, doi:[10.1017/jfm.2018.675](https://doi.org/10.1017/jfm.2018.675).
- [65] S. Karami, J. Soria, Analysis of coherent structures in an under-expanded supersonic impinging jet using spectral proper orthogonal decomposition (SPOD), *Aerospace* 5 (73) (2018) 73, doi:[10.3390/aerospace5030073](https://doi.org/10.3390/aerospace5030073).
- [66] D. Brouzet, A. Haghir, M. Talei, M.J. Brear, O.T. Schmidt, G. Rigas, T. Colonius, Role of coherent structures in turbulent premixed flame acoustics, *AIAA J.* 58 (6) (2020) 2635–2642, doi:[10.2514/1.j058480](https://doi.org/10.2514/1.j058480).
- [67] H. Sato, K. Amagai, M. Arai, Diffusion flames and their flickering motions related with Froude numbers under various gravity levels, *Combust. Flame* 123 (2000) 107–118, doi:[10.1016/S0010-2180\(00\)00154-1](https://doi.org/10.1016/S0010-2180(00)00154-1).
- [68] T. Poinso, D. Veynante, *Theoretical and numerical combustion*, third ed., RT Edwards, Inc., 2005.